37th AIAA Plasmadynamics and Lasers Conference
5 - 8 June 2006, San Francisco, California

AIAA 2006-2894

Simulation of MHD Turbulence-Chemistry Interaction in Supersonic Flow

Joey Schulz*, Kenji Miki†, and Suresh Menon‡
Georgia Institute of Technology,
Atlanta, GA, 30332-0150, USA

In order to improve the operational efficiency of scramjet engines, it is necessary to develop new techniques to increase the mixing and flameholding properties at high Mach numbers of current scramjet designs. This paper investigates the high-temperature chemistry and plasmadynamic effects of a discharge arc in a supersonic shear layer. This is the first step in developing a clear understanding of the physics governing flameholding and mixing in scramjets. Magnetohydrodyamic source terms are included in fluid conservation equations and the electron energy conservation equation is added to the solution set. This allows the modeling of additional terms such as Ohmic heating, ionization energy loss, and heat transfer through electron and heavy particle collision. The large-eddy simulation (LES) equations are derived and closed using a local-dynamic kinetic energy model (LDKM). The magnetohydrodynamic LES equations are solved numerically under the low Magnetic Reynolds assumption, and the magnetohydrodynamic subgrid terms are ignored in the current work, although these assumptions can be easily relaxed. A chemical kinetic model proposed by Chul Park, which uses 11 species and 51 reactions, simulates the radical distributions in the vicinity of the plasma. Results for a plasma source in a supersonic flow are discussed in this paper.

Nomenclature

$\bar{\rho}_e$	electron density
$\bar{\tau}_{ij}$	filtered viscous stress tensor
$\bar{C}_e$	average electron speed
$\bar{p}_e$	electron pressure ($= n_e k_B T_e$)
$\bar{q}_i$	filtered heat flux vector
$\Delta h'_{f,k}$	kth species heat of formation at reference temperature T^0
Δ	subgrid filter scale
$\dot{\omega}$	reaction rate of the kth species
$\Gamma_{e,h}$	electron-heavy particle collision frequency
κ	filtered mixture thermal conductivity
λ_e	electron mean free path
μ	molecular viscosity
μ_t	eddy viscosity at the grid filter level ($= \nu_t \bar{\rho}$)
ν_t	subgrid eddy viscosity
$\nu_{e,h}$	electron-heavy particle collision frequency per-unit time and volume
ρ	fluid mixture density
σ	electrical conductivity
$\tilde{D}_k$	kth species diffusion coefficient
$\tilde{E}$	filtered fluid specific energy

*Undergraduate Research Assistant, AIAA Student Member.
†Graduate Research Assistant, AIAA Student Member.
‡Professor, and Associate Fellow.

$\tilde{E}_e$	electron specific energy
$\tilde{h}_k$	kth species specific enthalpy
$\tilde{S}_ij$	resolved rate of strain
$c_{v,k}$	kth species specific heat at constant volume
e	electron charge (1.6×10^{-19})
H_i^{sgs}	total subgrid enthalpy flux
j	electron current density
k^{sgs}	subgrid kinetic energy
k_B	Boltzmann's constant
k_e	electron thermal conductivity
k_{test}	kinetic energy at the test filter level
L_{ij}	Leonard's Stress
m_e	mass of an electron
M_h	average mass of heavy particles
n_e	number of electrons per unit volume
n_h	number of heavy particles per unit volume
N_s	total number of species
p	fluid pressure
Pr_t	turbulent Prandtl number
$Q_{e,h}$	electron-heavy particle collision cross-section
R_k	kth species gas constant
Sc_t	turbulent Schmidt number
T	heavy particle mean temperature
T_d	activation temperature
T_e	electron temperature
T_v	vibrational temperature
u_i	fluid velocity
$Y_{i,k}^{sgs}$	kth subgrid convective species flux
Y_k	kth species mass fraction

I. Introduction

The use of electrical discharges in the field of aerodynamics has achieved much attention because they offer the potential ability to enhance the performance of many aerospace applications. The ability to supply a local heat source creating both highly energetic particles and radicals allows for the potential altering of the flow structure in an advantageous way. The renewed interest some years ago in the AJAX vehicle concept, developed by the Leninetz Company, brought to the forefront the consideration of many potential technologies involving electrical discharges.[1] This paper focuses on the use of electrical discharges in supersonic combustion.

The successful implementation and design of scramjet engines is essential to the development of an highly efficient single-stage-to-orbit (SSTO) space vehicle. One of the most important issues that still needs to be addressed in the design of a feasible scramjet is mixing enhancement and flame stabilization specifically at high combustor inlet Mach numbers. Mixing enhancement is necessary due to the short residence time of the fuel and air in the combustor.

A variety of approaches have been proposed that seek to enhance or maintain combustion in supersonic flow through the careful introduction of cavities, rearward-facing steps, and struts. These geometrical changes, or passive methods, do provide combustion enhancement through increased mixing, longer residence times, and flameholding.[2] However, these devices are static in nature and may be difficult to optimize for the entire range of Mach numbers that are of interest. A still more promising solution is the use of electrical discharges to create a localized high-density plasma. The plasma may provide a local source of heat and radicals advancing the chemical kinetics, increases mixing and thus enhancing combustor performance. From a design point of view, the plasma source may act as a virtual flameholder stabilizing the flame during transients. Furthermore, since the plasma location can be moved, this approach may be means to move this virtual flameholder(s) as needed by the operating conditions.

The types of electrical discharges can be classified as how the plasma ionizes and dissociates the gas. Arc

discharges, plasma torches, sustained radio frequency induced plasmas, and lasers supply large amounts of thermal energy (joule heating), typically resulting in high gas temperatures and highly favorable reaction rates. On the other hand, non-equilibrium plasmas including low-pressure glow, radio frequency, corona or barrier, microwave, and nano-second high-voltage discharges rely on highly energetic electron collisions and radical generation to enhance combustion. These discharges result in extremely large electron temperatures and only moderate mean flow temperature increases. Ideally, the plasma discharge should exist somewhere in between these two states in order to benefit from the high gas temperatures of the former and the high radical generation and more modest power requirements of the latter.[2] From experimental observation, Leonov has noted that electrical discharges existing in a non-equilibrium thermodynamic state and applied in a non-uniform manner offer the highest advantages in plasma-assisted combustion.[3]

The difficulty with plasma-assisted combustion is the large electrical power that may be required to enhance the chemical processes and problems associated with stability. Moreover, as a result of little computational and experimental data, there is no versatile solution to the design and application of plasma-assisted supersonic flameholding and combustion.[3] This paper addresses these issues by developing a new LES approach on the computational modeling of a plasma within a two-dimensional supersonic shear layer without combustion. The qualitative effects of the plasma on the flowfield are investigated and the total electrical power is calculated. The simulation reported here will focus primarily on the impact of this source on the high temperature supersonic air flow. The effect of a plasma source on the combustion processes will be investigated later.

II. Formulation

Simulations of a supersonic flow past step-combustor with and without plasma assistance are conducted using large-eddy simulations (LES). The governing equations for a multi-species, non-conducting, unsteady, compressible, reacting fluid are discussed in this section. For more details, please refer to the cited references.[4–6] The addition of the electron energy equation and the magnetohydrodynamic terms are discussed in this paper in subsequent sections.

A. LES Equations

The non-conducting flow variables are decomposed into the resolved and unresolved (subgrid-scale) components, such that $f = \tilde{f} + f''$, where the tilde represents the resolved scale and the double prime represents the unresolved subgrid scale quantities. The Favre filtered variable is defined as $\tilde{f} = \bar{\rho f}/\bar{\rho}$, where the overbar represents a spatial filtering.[6]

Applying the filtering to the conservation equations results in the following LES equations:

$$\frac{\partial \bar{\rho}}{\partial t} + \frac{\partial \bar{\rho}\tilde{u}_i}{\partial x_i} = 0 \tag{1}$$

$$\frac{\partial \bar{\rho}\tilde{u}_i}{\partial x_i} + \frac{\partial}{\partial x_j}\left[\bar{\rho}\tilde{u}_i\tilde{u}_j + \bar{p}\delta_{ij} - \bar{\tau}_{ij} + \tau_{ij}^{sgs}\right] = \widetilde{F_{s,i}} \tag{2}$$

$$\frac{\partial \bar{\rho}\tilde{E}}{\partial t} + \frac{\partial}{\partial x_i}\left[\left(\bar{\rho}\tilde{E} + \bar{p}\right)\tilde{u}_i + \bar{q}_i - \tilde{u}_j\bar{\tau}_{ij} + H_i^{sgs} + \sigma_i^{sgs}\right] = \widetilde{Q_s} \tag{3}$$

$$\frac{\partial \bar{\rho}\tilde{Y}_k}{\partial t} + \frac{\partial}{\partial x_i}\left[\bar{\rho}\tilde{Y}_k\tilde{u}_i + \bar{\rho}\tilde{Y}_k\tilde{V}_{i,k} + Y_{i,k}^{sgs} + \theta_{i,k}^{sgs}\right] = \bar{\omega}_k \tag{4}$$

where $k = 1, \ldots, N_s - 1$. All terms with superscript sgs denote subgrid quantities and require closure. The terms with the subscript s represent the magnetohydrodynamic source terms. These are discussed later. The filtered heat-flux, $\bar{q}_i$, is defined as:

$$\bar{q}_i = -\kappa\frac{\partial \tilde{T}}{\partial x_i} + \bar{\rho}\sum_{k=1}^{N_s}\bar{h}_k\bar{Y}_k\tilde{V_{i,k}} + \sum_{k=1}^{N_s}q_{i,k}^{sgs} \tag{5}$$

The filtered diffusion velocities are obtained using Fick's law, $\tilde{V_{i,k}} = \left(-\tilde{D}_k/\tilde{Y}_k\right)\left(\partial\tilde{Y}_k/\partial x_i\right)$. The pressure is determined from the filtered equation of state, $\bar{p} = \bar{\rho}\tilde{R}\tilde{T} + \bar{\rho}T^{sgs}$, and the filtered total energy per unit volume is $\bar{\rho}\tilde{E} = \bar{\rho}\tilde{e} + \frac{1}{2}\bar{\rho}\tilde{u}_i\tilde{u}_i + \bar{\rho}k^{sgs}$. Where $\tilde{R} = \sum_{k=1}^{N_s} R_k\tilde{Y}_k$ is the mixture gas constant, and $k^{sgs} = \frac{1}{2}[u_k\tilde{u}_k - \tilde{u}_k\tilde{u}_k]$, and the filtered internal energy is given by $\tilde{e} = \sum_{k=1}^{N_s}\left[c_{v,k}\tilde{Y}_k\tilde{T} + \tilde{Y}_k\delta h'_{f,k}\right]$.

The subgrid terms that require closure are

$$\tau_{ij}^{sgs} = \bar{\rho}\left(\widetilde{u_iu_j} - \tilde{u}_i\tilde{u}_j\right) \tag{6}$$

$$H_i^{sgs} = \bar{\rho}\left(\widetilde{Eu_i} - \tilde{E}\tilde{u}_i\right) + \left(\overline{pu_i} - \bar{p}\tilde{u}_i\right) \tag{7}$$

$$\sigma_i^{sgs} = \widetilde{u_j\tau_{ij}} - \tilde{u}_j\bar{\tau}_{ij} \tag{8}$$

$$Y_{i,k}^{sgs} = \bar{\rho}\left[\widetilde{u_iY_k} - \tilde{u}_i\tilde{Y}_k\right] \tag{9}$$

$$q_{i,k}^{sgs} = \left[\overline{h_kD_k\partial T_k/\partial x_i} - \tilde{h}_k\tilde{D}_k\partial\tilde{Y}_k/\partial x_i\right] \tag{10}$$

$$\theta_{i,k}^{sgs} = \rho\left[\widetilde{V_{i,k}Y_k} - \tilde{V}_{i,k}\tilde{Y}_k\right] \tag{11}$$

$$T^{sgs} = \sum_{k=1}^{N_s} R_k\left[\widetilde{Y_kT} - \tilde{Y}_k\tilde{T}\right] \tag{12}$$

B. Momentum Transport Closure

The subgrid-stress tensor τ_{ij}^{sgs} is closed using a subgrid eddy viscosity and gradient diffusion model at the grid cutoff scale:

$$\tau_{ij}^{sgs} = -2\bar{\rho}\nu_t\left[\tilde{S}_{ij} - \frac{1}{3}\tilde{S}_{kk}\delta_{ij}\right] + \frac{2}{3}\bar{\rho}k^{sgs}\delta_{ij} \tag{13}$$

The resolved rate of strain is $\tilde{S}_{ij} = (1/2)(\partial\tilde{u}_i/\partial x_j + \partial\tilde{u}_j/\partial x_i)$, and ν_t is the subgrid eddy viscosity. A non-equilibrium subgrid kinetic energy k^{sgs} equation is used to determine the eddy viscosity and is given by:

$$\frac{\partial\bar{\rho}k^{sgs}}{\partial t} + \frac{\partial}{\partial x_i}\left(\bar{\rho}\tilde{u}_ik^{sgs}\right) = -\tau_{ij}^{sgs}\frac{\partial\tilde{u}_i}{\partial x_j} - C_\epsilon\bar{\rho}\frac{(k^{sgs})^{\frac{3}{2}}}{\bar{\Delta}} + \frac{\partial}{\partial x_i}\left(\bar{\rho}\frac{\nu_t}{C_t}\frac{\partial k^{sgs}}{\partial x_i}\right) \tag{14}$$

The subgrid eddy viscosity is modeled as $\nu_t = C_\nu\bar{\Delta}(k^{sgs})^{1/2}$, where $\bar{\Delta} = (\Delta x\Delta y\Delta z)^{1/3}$ is based on the local grid size $(\Delta x, \Delta y, \Delta z)$. The coefficients C_ν, C_ϵ, and C_t are obtained using a localized dynamic procedure for the subgrid kinetic energy model (referred to as LDKM), as briefly summarized below.

This dynamic procedure takes advantage of the self-similarity of the subgrid-stress τ_{ij}^{sgs} at the grid filter level $\bar{\Delta}$ and the Leonard's stress $L_{ij}(= [\langle\bar{\rho}\tilde{u}_i\tilde{u}_j\rangle - \langle\bar{\rho}\tilde{u}_i\rangle\langle\bar{\rho}\tilde{u}_j\rangle]/\hat{\bar{\rho}})$ at the test filter level $\hat{\Delta}(= 2\bar{\Delta})$. Both $\hat{f}$ and $\langle f\rangle$ represent test filtering. The subgrid kinetic energy at the test level, $\hat{\tau}_{ij}^{sgs}$ is determined in the same manner as τ_{ij}^{sgs} above. Since the Leonard stress can be computed at the test filter, if we define the subgrid kinetic energy at the test filter as $k_{test} = \frac{1}{2}[\bar{\rho}\hat{\tilde{u}_k}^2/\hat{\bar{\rho}} - \bar{\rho}\hat{\tilde{u}_k}^2/\hat{\bar{\rho}}^2]$, the coefficient C_ν can be determined by: $(\hat{C_L} = 1)$

$$L_{ij} = \hat{\tau}^{sgs}/\hat{C_L} = -2\hat{\bar{\rho}}(C_\nu/\hat{C_L}\sqrt{k_{test}}\hat{\Delta}\left(\langle\tilde{S_{ij}}\rangle - \frac{1}{3}\langle\tilde{S_{kk}}\rangle\delta_{ij}\right) + \frac{2}{3}\left(1/\hat{C_L}\right)\hat{\bar{\rho}} \sim k_{test}\Delta_{ij} \tag{15}$$

The value of C_ν is determined from the above equation using a least-square method. Thus,

$$C_\nu = -\frac{L'_{ij}M_{ij}}{2M_{ij}M_{ij}} \tag{16}$$

Here, $L'_{ij} = L_{ij} - \frac{2}{3}\hat{\bar{\rho}}k_{test}\delta_{ij}$ and $M_{ij} = \hat{\bar{\rho}}\sqrt{k_{test}}\hat{\Delta}\left(\langle\tilde{S}_{ij}\rangle - \frac{1}{3}\langle\tilde{S}_{kk}\rangle\Delta_{ij}\right)$. A similar approach is used to solve for C_ϵ.

$$C_\epsilon = \frac{\hat{\Delta}(\mu+\mu_t)}{\hat{\bar{\rho}}k_{test}^{\frac{3}{2}}}\left[\langle\tilde{T_{ij}}\frac{\partial\tilde{u}_j}{\partial x_i}\rangle - \hat{\tilde{T_{ij}}}\frac{\partial\hat{\tilde{u}}_j}{\partial x_i}\right] \tag{17}$$

where the tensor $\tilde{T_{ij}}$ is defined as $[\partial\tilde{u_i}/\partial x_j + \partial\tilde{u_j}/\partial x_i - \frac{2}{3}(\partial\tilde{u_k}/\partial x_k)\delta_{ij}$ and $\hat{\tilde{T_{ij}}}$ indicates the tensor at the test-filter level.

C. Energy and Scalar Transport Closure

The other subgrid terms are closed using the eddy viscosity and a gradient assumption as

$$H_i^{sgs} = -\bar{\rho}\frac{\nu_t}{Pr_t}\frac{\partial\tilde{H}}{\partial x_i} \tag{18}$$

where the filtered total enthalpy is the sum of the specific enthalpy of mixture, specific kinetic energy, and specific subgrid-scale energy: $\tilde{H} = \tilde{h} + (1/2)\tilde{u}_i\tilde{u}_j + k^{sgs}$, where

$$\tilde{h} = \sum_{k=1}^{N_s}\tilde{h}_k\tilde{Y}_k \tag{19}$$

In a similar fashion,

$$Y_{i,k}^{sgs} = -\frac{\bar{\rho}\nu_t}{Sc_t}\frac{\partial\tilde{Y}_k}{\partial x_i} \tag{20}$$

The subgrid terms σ_i^{sgs}, q_i^{sgs}, T^{sgs}, and $\theta_{i,k}^{sgs}$ are usually neglected in the LES model.[7] The magnetohydrodynamic subgrid terms and the subsequent closure equations are not included in this paper. However, their closure is discussed elsewhere.[8] These terms do not influence the flow field in this application due to the low conductivity of the medium and the small isolated region of charged particles.

D. Magnetohydrodynamic Governing Equations

In order to capture the physics of conducting flows, the Lorentz force and an electron-heavy particle coupling term are added to the governing LES equations. The source terms are added only to the resolved equations. The magnetohydrodynamic source term in Equation 2 is the Lorentz force and is generally written in vector notation as $\vec{J}\times\vec{B}$. This term does not affect the flow significantly in the application investigated in this paper. Two source terms are added to the resolved energy conservation equation, Equation 3. A collisional heat transfer source term and a radiative loss source term. The former represents the conductive heat transfer between the highly energetic electrons and the surrounding uncharged species. This term is equal to $-\Delta\dot{\epsilon}_{e,h}$ and is given by Equation 23. The radiative loss term accounts for the loss of energy in the system during a radiative recombination reaction due to the escape of a photon. The photon energy is estimated to be approximately the energy of the absorbed electron. The radiative losses are governed by the reaction rates of the radiative recombination reactions discussed in the next section. These reaction rates are given in Table I of the Appendix.

Leonov[3] states that the plasma affects the flow structure by the ohmic heating of medium surrounding the plasma and the non-equilibrium excitation and dissociation of the medium as a result of electron collisions and UV radiation. The later requires the use of a two-temperature energy equation model to accurately describe the non-equilibrium condition between the heavy particles and the electrons. The energy equation for the electrons is given below:[9–11]

$$\frac{\partial\rho_e\tilde{E}_e}{\partial t} = -\frac{\partial\tilde{E}_e u_i}{\partial x_i} - \bar{p}_e\frac{\partial u_i}{\partial x_i} + \frac{j^2}{\sigma} - \Delta\dot{\epsilon}_{e,h} + \frac{\partial}{\partial x_j}\left(k_e\frac{\partial T_e}{\partial x_i}\right) - \sum_{k=1}^{N_s}\omega_{k+1}\chi_{i\rightarrow i+1} \tag{21}$$

where $\tilde{E}_e$ is the electron energy per mass, $\bar{p}_e$ is the electron pressure, defined by the equation of state $\bar{p}_e = n_e k_B T_e$, χ is the ionization energy, and ω_k is the reaction source term defined as the rate of production minus the rate of destruction of the species.

The third term in the above energy equation is the ohmic or resistive heating. The electric conductivity (σ) is the function of the electron density and collision frequency($=\Gamma_{e,h}$):

$$\sigma = \frac{e^2 n_e^2}{2 m_e \Gamma_{e,h}} \tag{22}$$

The fourth term represents the heat transfer between heavy particle and electron due to the binary collision and is defined by:[11]

$$\triangle \dot{\epsilon}_{e,h} = \frac{3\bar{\rho}_e \nu_{e,h}}{M_h} k_B (\tilde{T}_e - \tilde{T}) \tag{23}$$

where ρ_e is the electron density, and $\nu_{e,h}$ is the collision frequency of an electron per unit volume and time and is $\nu_{e,h} = \Gamma_{e,h}/n_e = \frac{1}{2}\bar{C}_e n_h \Sigma Q_{e,h}$, where $\bar{C}_e$ is the average speed of electron$(= \sqrt{8k_B T_e/(\pi M_e)})$. Also, n_h is the heavy particle mass density, and $Q_{e,h}$ is the collisional cross section. The assumption is made that $Q_{e,h} \approx Q_{e,h+}$ and determined by experimental data.[12] The thermal coefficient is calculated from kinetic theory, $k_e = \frac{1}{3}\bar{C}_e n_e k_B \lambda_e$, where λ_e is the emean free path determined from $\lambda_e = \frac{1}{\Sigma(n_h Q_{e,h})}$, and compared to experimental data for verification.[13] The last term describes the energy loss of electron due to electron-impact ionization process.

During an ionization reaction, the incident particle loses a of increment of energy associated with the ionization energy of the atom. The newly-born electron has a negligibly small amount of energy and only contributes to the overall electron density. The recombination energy loss associated with a ionized heavy particle capturing an electron is assumed to be the same as the electron's thermal energy.

III. Chemical Kinetic Model

Park[14] provides a detailed chemical kinetic mechanisms for high temperatures gases using a two-temperature model. The model considers 11 species $(N, N^+, O, O^+, N_2, N_2^+, O_2, O_2^+, NO, NO^+, e^-)$ and 51 reactions. These are listed for reference in Table I of the Appendix. There are three types of ionic reactions that must be considered in combination the dissociation and recombination reactions: 1) associative ionization, 2) charge-exchange, and 3) electron-impact ionization. Electrons are first produced by the associative ionization process $N + O \rightarrow NO^+ + e^-$. When the resulting density of electrons is large enough, electron collisions with neutral species become frequent, and an electron avalanche occurs.[14] The ionization of O and N and the radiative recombination reactions reduce the electron temperature.

The reaction rate coefficients are calculated using the following Arrhenius form:

$$k_f = C T_x^n exp(-T_d/T_x) \tag{24}$$

where T_x is the controlling temperature (T, T_a, T_e, or T_v) and T_d is the activation temperature. The coefficients C and n are specified in Table I of the Appendix. The arithmetic mean temperature is $T_a = T^{0.5} T_v^{-0.5}$ and is used for the controlling temperature of the dissociation reactions. For the purpose of the model, the electron temperature T_e is assumed to be equal to the vibrational temperature T_v. The coefficients and the correct controlling temperatures were determined by correlation to experimental data collected at super-escape velocities. All data is summarized in Table I of the Appendix.[14–16]

The back reactions are determined from the equilibrium coefficients computed by Park using the form: $K_e = exp[A_1/Z + A_2 + A_3 \ln(Z) + A_4 Z + A_5 Z^2]$ where $Z = 10,000/T$. The coefficients are given in Table 2 of the Appendix.[17] The equilibrium concentration for the 10 species at an electron temperature of 10,000 K is shown in Fig. 3.

The requirement of quasi-neutrality and charge conservation implies that the electron density is simply the sum of all the charged particles:

$$n_e = \sum_{i=1}^{5} n_i \tag{25}$$

IV. Numerical Methods

An explicit time integration, finite-volume solver that uses uses a Piecewise Parabolic method (PPM, Woodward and Colella, 1984)[18] for the inviscid fluxes is used for solving the conservation equations. For more information, please refer to the cited references.[19] As a summary, the full set of conservation equations solved are expressed in divergence form.

$$\frac{\partial \vec{Q}}{\partial t} + \nabla \cdot \vec{F} = \vec{S} \tag{26}$$

where the vector $\vec{Q} = (\bar{\rho},\ \bar{\rho}\tilde{u},\ \bar{\rho}\tilde{v},\ \bar{\rho}\tilde{w},\ \bar{\rho}\tilde{E},\ \bar{\rho}\tilde{Y}_k,\ \bar{\rho}_{elec}\tilde{E}_{elec})^T$ and the vector $\vec{S} = (0,\ 0,\ 0,\ 0, -\Delta\dot{\epsilon}_{e,h} - R,\ \omega_k,\ P_{E,elec} - D_{E,elec})^T$ where $-R$ is the radiation recombination loss. The terms $P_{E,elec}$ and $D_{E,elec}$ are defined by:

$$\begin{cases} P_{E,elec} = \frac{j^2}{\sigma} + \nabla \cdot (k_e \bigtriangledown T_e) \\ D_{E,elec} = \triangle\dot{\epsilon}_{e,h} + p_e \nabla \cdot \vec{u} + \sum \omega_{k+1}\chi_{k\rightarrow k+1} \end{cases} \tag{27}$$

and the vector $\vec{F}$ is the flux of $\vec{Q}$ written as,

$$F = F_x + F_y + F_z \tag{28}$$

where

$$F_x = \begin{pmatrix} \bar{\rho}\tilde{u} \\ \bar{\rho}\tilde{u}\tilde{u} + \bar{p} \\ \bar{\rho}\tilde{u}\tilde{v} \\ \bar{\rho}\tilde{u}\tilde{w} \\ (\bar{\rho}\bar{E} + \bar{p})\tilde{u} \\ \bar{\rho}\tilde{u}\tilde{Y}_k \\ \bar{\rho}\tilde{u}E_e \end{pmatrix} + \begin{pmatrix} 0 \\ \tau_{xx} + \tau_{xx}^{sgs} \\ \tau_{xy} + \tau_{xy}^{sgs} \\ \tau_{xz} + \tau_{xz}^{sgs} \\ \tilde{u}\tau_{xx} + \tilde{v}\tau_{xy} + \tilde{w}\tau_{xz} - \bar{q}_x - H_x^{sgs} - \sigma_x^{sgs} \\ -\bar{\rho}\tilde{Y}_k\tilde{V}_{x,k} - Y_{x,k}^{sgs} - \theta_{x,k}^{sgs} \\ k_e(\nabla T_e) \end{pmatrix} \tag{29}$$

$$F_y = \begin{pmatrix} \bar{\rho}\tilde{v} \\ \bar{\rho}\tilde{v}\tilde{u} \\ \bar{\rho}\tilde{v}\tilde{v} + \bar{p} \\ \bar{\rho}\tilde{v}\tilde{w} \\ (\bar{\rho}\bar{E} + \bar{p})\tilde{v} \\ \bar{\rho}\tilde{v}\tilde{Y}_k \\ \bar{\rho}\tilde{v}\bar{E}_e \end{pmatrix} + \begin{pmatrix} 0 \\ \tau_{yx} + \tau_{yx}^{sgs} \\ \tau_{yy} + \tau_{yy}^{sgs} \\ \tau_{yz} + \tau_{yz}^{sgs} \\ \tilde{u}\tau_{yx} + \tilde{v}\tau_{yy} + \tilde{w}\tau_{yz} - \bar{q}_y - H_y^{sgs} - \sigma_y^{sgs} \\ -\bar{\rho}\tilde{Y}_k\tilde{V}_{y,k} - Y_{y,k}^{sgs} - \theta_{y,k}^{sgs} \\ k_e(\nabla T_e) \end{pmatrix} \tag{30}$$

$$F_z = \begin{pmatrix} \bar{\rho}\tilde{w} \\ \bar{\rho}\tilde{w}\tilde{u} \\ \bar{\rho}\tilde{w}\tilde{v} \\ \bar{\rho}\tilde{w}\tilde{w} + \bar{p} \\ (\bar{\rho}\bar{E} + \bar{p})\tilde{w} \\ \bar{\rho}\tilde{w}\tilde{Y}_k \\ \bar{\rho}\tilde{w}E_e \end{pmatrix} + \begin{pmatrix} 0 \\ \tau_{zx} + \tau_{zx}^{sgs} \\ \tau_{zy} + \tau_{zx}^{sgs} \\ \tau_{zz} + \tau_{zx}^{sgs} \\ \tilde{u}\tau_{zx} + \tilde{v}\tau_{zy} + \tilde{w}\tau_{zz} - \bar{q}_z - H_z^{sgs} - \sigma_z^{sgs} \\ -\bar{\rho}\tilde{Y}_k\tilde{V}_{z,k} - Y_{z,k}^{sgs} - \theta_{z,k}^{sgs} \\ k_e(\nabla T_e) \end{pmatrix} \tag{31}$$

A. Initial Conditions

The proper initial conditions are critical for numerical stability. The stability of the plasma is dependent upon the temperature and concentration of the electrons and the heavy particles. If the electron density decreaseas too much, the plasma will extinguish. In order to avoid this, a numerical scheme controls the electron density and temperature by changing the input current. Steady-state is achieved when the input power is constant. For reference, Leonov[3] has observed mean gas temperatures around 3000 K and electron temperatures of approximately 10,000 K. The dimensions of the simulation domain are shown in Fig. 2. The grid resolution is 350×250. The grid spacing is clustered around the plasma source in order to resolve the large temperature gradients.

B. Limitations of the Model

The CHEMKIN database is used to determine the specific heats of all heavy particles. This set of data is valid for gas temperatures below 5000 K. The specific heat of the electrons is constant and valid at any temperature. The heavy particle temperature does not exceed 5000 K at the power levels considered in this paper.

The coefficient of viscosity for each species is determined from experimental data of an air mixture. Therefore, all particles have the same coefficient of viscosity. This not influence the validity of our results to a very high degree. The same data is used to determine the Prandtl number. The Lewis number for ionized species is assumed to be near that of the neutral species.

Kinetic thoery is used to derive an expression for the thermal conductivity of the electrons and should be valid in the temperature range considered in this paper. The thermal conductivity of the heavy particles is determined form experimental data in the same manner as the viscosity.

The electrical conductivity is determined using kinetic theory. The cross-sectional data was compiled by Bose for many species and is used in this simulation.[12]

C. Numerical Results

A plasma source is simulated in a two-dimensional step combustor with an inflow velocity of 500 meters per second, approximately Mach 1.5. The source is located in the shear layer just aft of the step. A schematic of the simulation setup is shown Fig. 2. Fig. 4 a shows the $x-$component of velocity for a simulation without the plasma source. Fig. 5a shows the density for the same case. The shear layer is evident. The expansion waves and the reflecting shock, which are typical of supersonic step-combustors, is evident by the pressure contours shown in Fig. 6a. The temperature contour is shown in Fig. 7a.

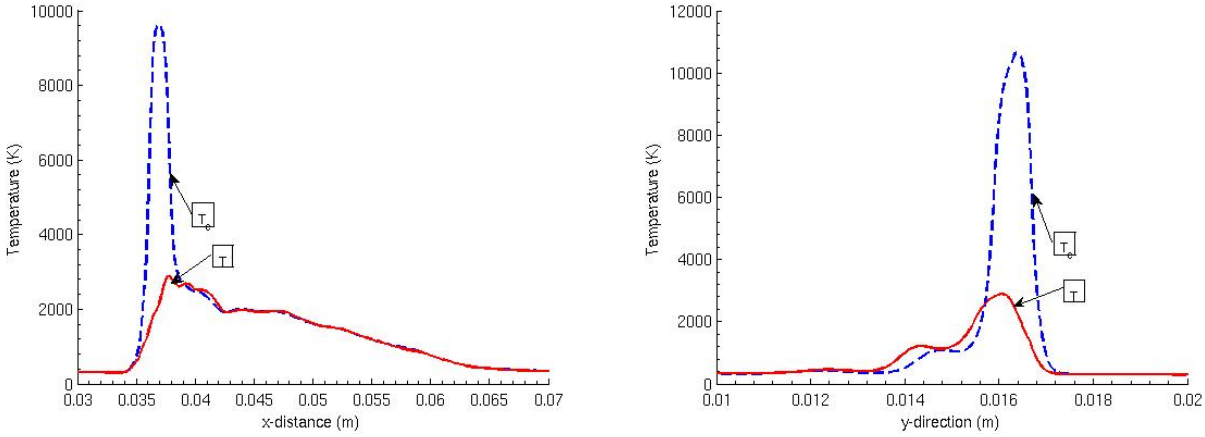

(a) Profile in x-direction

(b) Profile in y-direction

Figure 1. Temperature profiles near the plasma source. The maximum electron temperature is approximately 11,000 K and the maximum temperature of the heavy particles is around 3000 K.

The plasma discharge creates a source of highly energetic electrons that heat the heavy particles through collisions. The two species are in thermodynamic non-equilibrium as exhibited by Fig. 1. The heavy particle

and electron temperatures are near the temperatures observed in experimental measurements by Leonov.[3] As mentioned above, a non-equilibrium state seems to offer the largest potential for plasma-assisted combustion.

In this simulation, the plasma source smoothes out the shear layer. The shear layer does not spread as much when the plasma source is present. Without the plasma source, the shear layer spreads as excepted and eventually would reflect off the bottom wall. This does not occur when the plasma is present. The thermodynamic expansion of the plasma increases the velocity of the flow in the cavity and consequently dampens the vortical structures that would typically develop. Moreover, less expansion occurs when the plasma is present. The maximum velocity when the plasma is not present is around 630 m/s, but when the plasma source is present the maximum velocity is a little less than 600 m/s. The velocity contours of the two cases are shown in Fig.4 at the same scale.

The temperature of the plasma source fluctuates throughout the simulation. There is no reason to believe that this is non-physical, and in fact it should be expected. The temperature of heavy particles change as a result of the vortex shedding of the reward-facing step. These changes in temperature create pressure waves that reflect off of the walls of the step. The crisscross pattern observed in Fig. 6 is the result.

The intensification of the pressure field results in an local increase in the baroclinic torque. The baroclinic torque is related to the turbulent mixing in the shear layer and is computed by $T_b = (\nabla\bar{p} \times \nabla\bar{\rho})/\rho^2$. The magnitude of this quantity for both cases with and without the plasma source are shown in Fig. 9.

V. Acknowledgment

This research is supported by NASA/GRC through the University Research Engineering and Technology Institute for Aeropropulsion and Power under Grant Cooperative Agreement Number NCC3-982.

VI. Conclusion

Plasma-assisted combustion is a promising solution to many of the difficulties faced in supersonic combustion. This paper investigates the affects of a non-equilibrium plasma on a supersonic flow over a rearward-facing step. The LES conservation equations for mass, momentum, energy, electron energy, and species concentration are used with the LDKM subgrid closure. A detailed kinetic model containing 11 species and 51 reactions is used to simulate the high-temperature gas effects. The results indicate that the plasma reduces the spreading of the shear-layer, but significantly alters the pressure distribution of the flow, which might be advantageous for combustion since it results in an increase in the baroclinic torque. In the future, the dependence on the the plasma location will be investigated to determine if a more opportune location may result in further flow enhancement features.

References

[1]Wie, D. V., Risha, D., and Suchomel, C., "Research issues resulting from an assessment of technologies for future hypersonic aerospace systems," *42nd AIAA Aerospace Sciences Meeting & Exihibit, AIAA-2004-1357*, 2004.

[2]Ombrello, T., Qin, X., Ju, Y., Gustol, A., Fridmann, A., and Carter, C., "Combustion enhancement via Stabilized Piecewise Nonequilibrium Gliding Arc Plasma Discharge," *AIAA Journal*, Vol. 44, 2006, pp. 142–150.

[3]Leonov, S. B. and D.A.Yarantsev, "Plasma-Assisted Iginition and Flameholding in High-Speed Flow," *44th AIAA Aerospace Science, Meeting*, 2006.

[4]Kim, W.-W. and Menon, S., "An Unsteady Incompressible Navier-Stokes Solver for Large Eddy Simulation of Turbulent Flows," *International Journal for Numerical Methods in Fluids*, Vol. 31, 1999, pp. 983–1017.

[5]Kim, W.-W., Menon, S., and Mongia, H., "Large Eddy Simulation of a Gas Turbine Combustor Flow," *Combustion Science and Technology*, Vol. 143, 1999, pp. 25–62.

[6]Menon, S. and Patel, N., "Subgrid Modeling for Simulation of Spray Combustion in Large-Scale Combustors," *AIAA Journal*, Vol. 44, 2006, pp. 709–723.

[7]Fureby, C. and Moller, S., "On Large Eddy Simulation of Reacting Flows Applied to Bluff Body Stabilized Flames," *AIAA Journal*, Vol. 33, 1995, pp. 2339–2347.

[8]Miki, K. and Menon, S., "Local Dynamic Subgrid Closure for Compressible MHD Turbulence Simulation," *37th Plasmadynamics and Lasers Conference, AIAA-2006-2891*, 2006.

[9]J.Heirrmann and M.A.Kurtz, "Numerical and Experimental Investiogation of the current distribution in self-field MHD thrusters," *Journal of Propulsion and Power*, Vol. 21, 2005, pp. 119–127.

[10]M.A.Kurtz, S. and J.Heirrmann, "Energy partition in Inductively Heated Plasma Source for Reentry simulation," *Journal of Thermophysics and heat transfer*, Vol. 14, 2000, pp. 388–395.

[11]E.Y.Choueiri, K. and S.C.Jardin, "Application for a New numerical solver to the Simulation of MPD Flows," *44th AIAA Aerospace Science*, 2000.

[12]Bose, T. K., "High temperature gas dynamics," *Springer*, 2004.

[13]R.S.Devoto, "Electron transport properties in high-temperature," *The Physics of Fluids*, Vol. 19, 1975, pp. 22–24.

[14]Park, C., "Review of Chemical-Kinetic Problems of Future NASA Mission," *Journal of thermophysics and heat transfer*, Vol. 7, 1993, pp. 385–398.

[15]Park, C., *Nonequilibrium Hypersonic Aerothermodynamics*, John Wiley and Sons, 1990.

[16]I.V.Kochetov, N. E. and N.A.Dyatko, "The ionization kinetic and electric field in the leasder channel in lomg air gaps," *Journal of Physics.D.Applied Physics*, Vol. 30, 1997, pp. 1616–1624.

[17]Park, C., Jaffe, R. L., and Patridge, H., "Chemical-Kinetic Parameters of Hyperbolic Earth Entry," *Journal of Thermophysics and Heat Transfer*, Vol. 15, 2001, pp. 76–89.

[18]Woodward, P. and Colella, P., "The Numerical Simulation of Two-Dimensional Fluid Flow with Strong Shocks," *Journal of Computational Physics*, Vol. 54, 1984, pp. 115–173.

[19]Fryxell, B. and Menon, S., "Hybrid Simulations of Richtmyer-Meshkov Instability," *43rd Aerospace Sciences Meeting and Exhibit, AIAA-2005-0314*, 2005.

[20]Park, C., "A Review of Reaction Rates in High Temperature Air," *AIAA 24th Thermophysics Conference, AIAA-1989-1740*, 1989.

VII. Figures

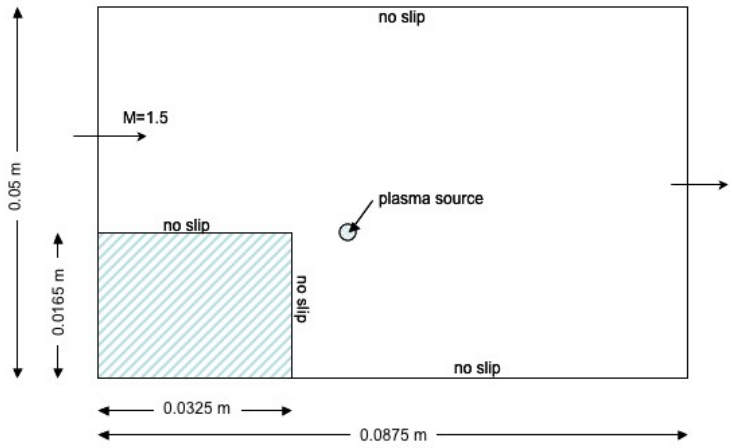

Figure 2. Schematic of the numerical setup

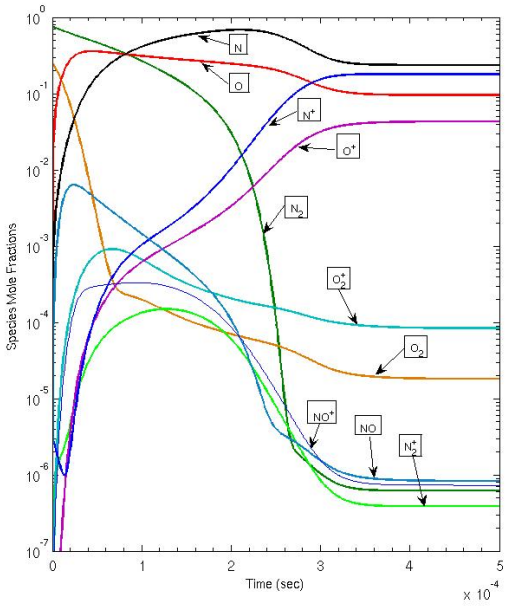

Figure 3. Equilibrium concentration at $T_e = 10,000K$ and $\rho = 1 \times 10^{-4}$

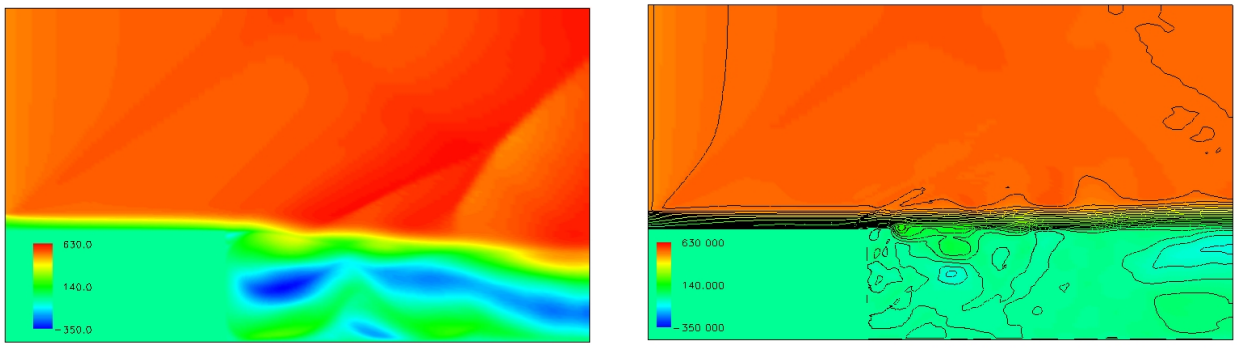

(a) Without Plasma Source

(b) With Plasma Source

Figure 4. Comparison of the velocity field with and without plasma source in supersonic step combustor

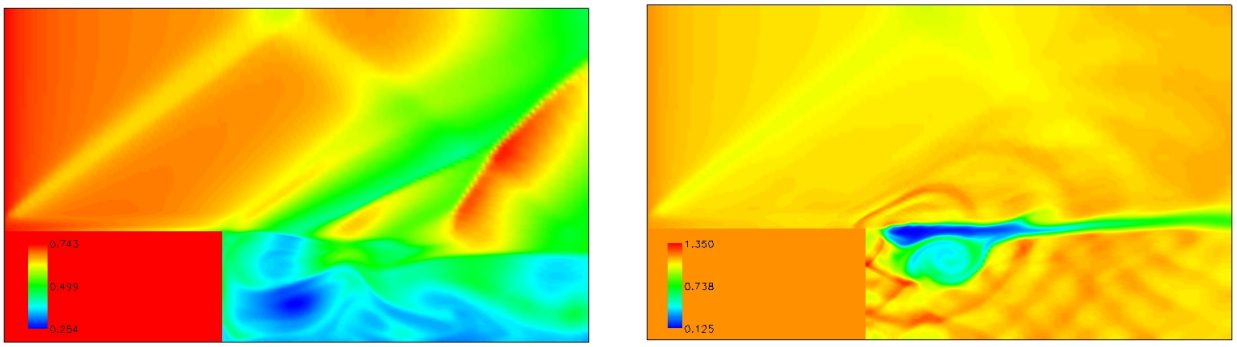

(a) Without Plasma Source (b) With Plasma Source

Figure 5. Comparison of the density contours with and without plasma source in supersonic step combustor (contour scales are not identical)

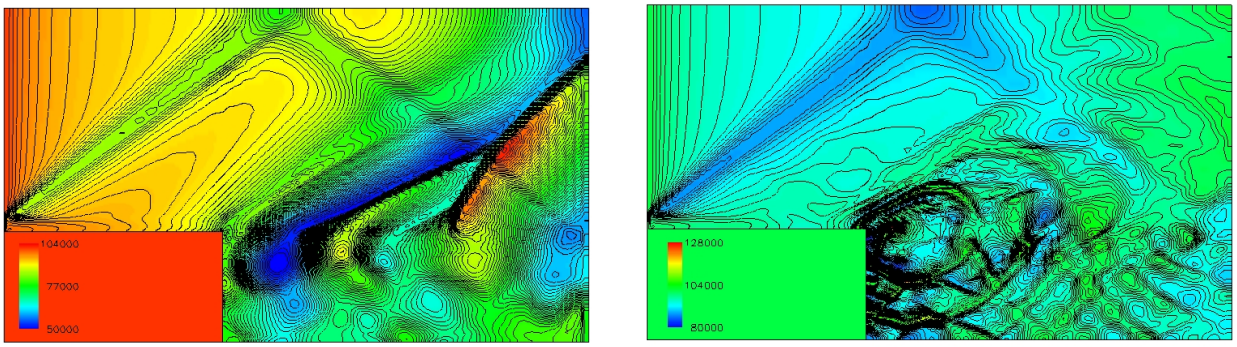

(a) Without Plasma Source (b) With Plasma Source

Figure 6. Comparison of the pressure field with and without plasma source in supersonic step combustor (contour scales are not identical)

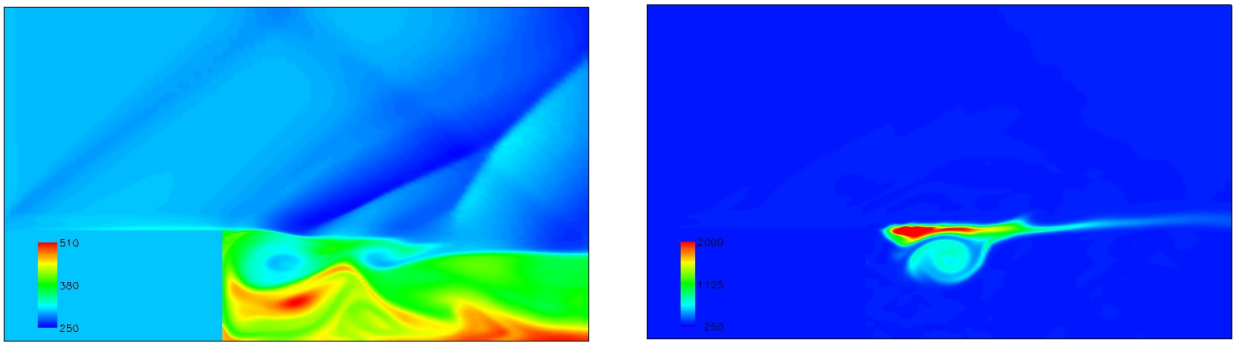

(a) Without Plasma Source (b) With Plasma Source

Figure 7. Comparison of the temperature contours with and without plasma source in supersonic step combustor (contour scales are not identical)

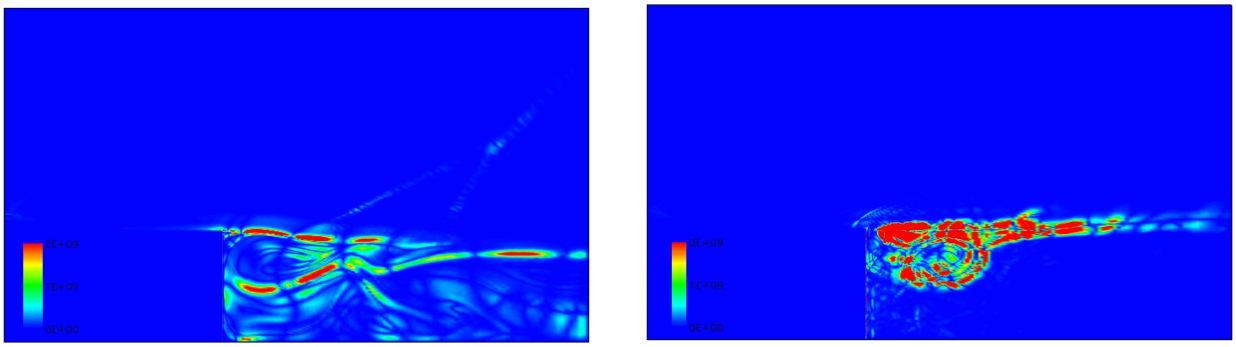

(a) Without Plasma Source

(b) With Plasma Source

Figure 8. Comparison of the magnitude of the Baroclinic Torque contours with and without plasma source in supersonic step combustor

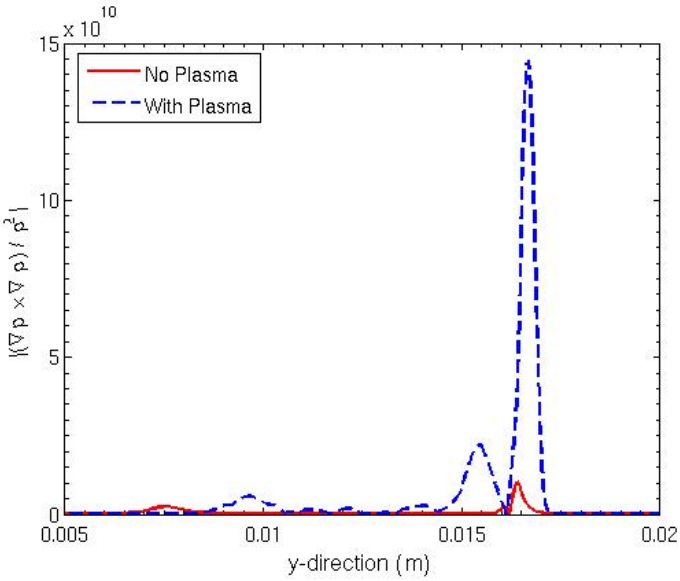

Figure 9. Comparison of the magnitude of the baroclinic torque term in the y-direction

A. High Temperature Gas Kinetic Mechanisms

Table 1: High Temperature Gas Kinetics from references[14, 15, 20]

Reaction	M	T_x^a	C	n	T_d
Dissociation Reactions					
$N_2 + M \rightarrow N + N + M$	N	T_a	3.0×10^{22}	-1.60	$113,200$
	O		3.0×10^{22}		
	N_2		7.0×10^{21}		
	O_2		7.0×10^{21}		
	NO		3.0×10^{22}		
	N^+		3.0×10^{22}		
	O^+		3.0×10^{22}		
	N_2^+		7.0×10^{21}		
	O_2^+		7.0×10^{21}		
	NO^+		7.0×10^{21}		
	e^-	T_e	1.2×10^{25}		
$O_2 + M \rightarrow O + O + M$	N	T_a	1.0×10^{22}	-1.50	$59,500$
	O		1.0×10^{22}		
	N_2		2.0×10^{21}		
	O_2		2.0×10^{21}		
	NO		2.0×10^{21}		
	N^+		1.0×10^{22}		
	O^+		1.0×10^{22}		
	N_2^+		2.0×10^{21}		
	O_2^+		2.0×10^{21}		
	NO^+		2.0×10^{21}		
$NO + M \rightarrow N + O + M$	N	T_a	1.1×10^{17}	0.00	$75,500$
	O		1.1×10^{17}		
	N_2		5.0×10^{15}		
	O_2		5.0×10^{15}		
	NO		2.0×10^{17}		
	N^+		1.1×10^{17}		
	O^+		1.1×10^{17}		
	N_2^+		5.0×10^{15}		
	O_2^+		5.0×10^{15}		
	NO^+		5.0×10^{15}		
NO Exchange Reactions					
$N_2 + O \rightarrow N + O_2$		T	8.4×10^{12}	0.00	$19,450$
$NO + O \rightarrow NO + N$		T	6.4×10^{17}	-1.00	$38,400$
Associative Ionization Reactions					
$N + O \rightarrow NO^+ + e^-$		T	8.8×10^{8}	1.00	$31,900$
$O + O \rightarrow O_2^+ + e^-$		T	7.1×10^{2}	2.70	$80,600$
$N + N \rightarrow N_2^+ + e^-$		T	4.4×10^{7}	1.50	$67,500$
Charge Exchange Reactions					
$NO^+ + O \rightarrow N^+ + O_2$		T	1.0×10^{12}	0.50	$77,200$
$N^+ + N_2 \rightarrow N_2^+ + N$		T	1.0×10^{12}	0.50	$12,200$
$O_2^+ + N \rightarrow N^+ + O_2$		T	8.7×10^{13}	0.14	$28,600$
$O^+ + NO \rightarrow N^+ + O_2$		T	1.4×10^{5}	1.90	$26,600$
$O_2^+ + N_2 \rightarrow N_2^+ + O_2$		T	9.9×10^{12}	0.00	$40,700$
$O_2^+ + O \rightarrow O^+ + O_2$		T	4.0×10^{12}	-0.09	$18,000$
$NO^+ + N \rightarrow O^+ + N_2$		T	3.4×10^{13}	-1.08	$12,800$
$NO^+ + O_2 \rightarrow O_2^+ + NO$		T	2.4×10^{13}	0.41	$32,600$
$NO^+ + O \rightarrow O_2^+ + N$		T	7.2×10^{12}	0.29	$48,600$
$O^+ + N_2 \rightarrow N_2^+ + O$		T	9.1×10^{11}	0.36	$22,800$
$NO^+ + N \rightarrow N_2^+ + O$		T	7.2×10^{13}	0.00	$35,500$
Electron-Impact Ionization Reactions					
$O + e^- \rightarrow O^+ + e^- + e^-$		T_e	3.9×10^{33}	-3.78	$158,500$
$N + e^- \rightarrow N^+ + e^- + e^-$		T_e	2.5×10^{34}	-3.82	$168,600$

continued from above.....

Reaction	M	T_x^a	C	n	T_d
Radiative Recombination Reactions					
$O^+ + e^- \rightarrow O + h\nu$		T_e	1.07×10^{11}	-0.52	0.00
$N^+ + e^- \rightarrow N + h\nu$		T_e	1.52×10^{11}	-0.48	
Recombination Reactions					
$N + O \leftarrow NO^+ + e^-$		T_e	9×10^{18}	-0.65	0.00
$N + N \leftarrow N_2^+ + e^-$		T_e	2.7×10^{18}	-0.5	
$O + O \leftarrow O_2^+ + e^-$		T_e	1.5×10^{18}	-0.5	

Table 2: High Temperature Gas Equilibrium Kinetics from references[15,17]

Reaction	A_1	A_2	A_3	A_4	A_5
$N_2 + M = N + N + M$	-3.293682	0.998998	-8.237028	-5.526183	-0.582174
$O_2 + M = O + O + M$	1.578640	2.688744	4.215573	-8.091354	0.174260
$N_2 + e^- = N + N + e^-$	-3.293682	0.998998	-8.237028	-5.526183	-0.582174
$N_2 + O = NO + N$	-3.032198	0.078468	-7.693047	1.411299	-0.517448
$NO + O = O_2 + N$	-1.840133	-1.768215	-4.759554	1.153872	-0.238985